coatings

MDPI

Article

Effect of Zn on Phase Evolution and Shear Resistance of Stainless Steel and Aluminum Alloy Interface by Laser Cladding

Keyan Wang [1], Xianqing Yin [1,*], Chengxin Li [1] and Kaiping Du [2]

[1] State Key Laboratory for Mechanical Behavior of Materials, School of Materials Science and Engineering, Xi'an Jiaotong University, Xi'an 710049, China; wangkeyantc@stu.xjtu.edu.cn (K.W.); licx@xjtu.edu.cn (C.L.)
[2] BGRIMM Technology Group, Beijing 100160, China; dukaiping@bgrimm.com
* Correspondence: xqyin@mail.xjtu.edu.cn

Abstract: The connection between aluminum and iron alloys is of immense significance in the pursuit of lightweight industrial products. However, the Fe-Al interface's inherent weakness restricts its widespread application. This study investigates the impact of Zn at the interface of Al-Fe laser cladding on the phase and mechanical properties of the interface. Specifically, we examine the influence of the applied Zn powder layer and alloying Zn layer on the morphology of the Fe-based cladding layer. The inclusion of Zn enhances the spreadability of the Fe-based cladding layer. Additionally, we elucidate the effect of Zn on the composition and phase of the Fe-Al laser cladding interface. Notably, the affinity between Zn and the η phase surpasses that of the θ phase, and an increased Zn content significantly thickens the η phase. Shear tests reveal that the failure mode of shear fracture encompasses both brittle and ductile fractures. Density functional theory (DFT) calculations indicate that Zn has a limited effect on the strength of the η phase but reduces the enthalpy of formation of the η phase. Our findings demonstrate that the alloyed Zn layer initially facilitates the formation of a continuous and uniform η layer, while an increased Zn content enhances and stabilizes the shear strength of the interface.

Keywords: laser cladding; dissimilar joining; interface; intermetallic compounds

check for updates

Citation: Wang, K.; Yin, X.; Li, C.; Du, K. Effect of Zn on Phase Evolution and Shear Resistance of Stainless Steel and Aluminum Alloy Interface by Laser Cladding. *Coatings* **2023**, *13*, 1267. https://doi.org/10.3390/coatings13071267

Academic Editor: Michał Kulka

Received: 20 May 2023
Revised: 26 June 2023
Accepted: 12 July 2023
Published: 19 July 2023

Copyright: © 2023 by the authors. Licensee MDPI, Basel, Switzerland. This article is an open access article distributed under the terms and conditions of the Creative Commons Attribution (CC BY) license (https://creativecommons.org/licenses/by/4.0/).

1. Introduction

Aluminum alloys have compelling potential as a substitute for traditional steel but require surface strengthening to broaden their applications due to their lower hardness. Laser cladding offers an efficient and versatile technology that can create a high-hardness metal cladding layer on the surface of aluminum alloy, improving its wear resistance and thus making it more suitable for various uses such as automotive lightweighting and electric vehicle battery manufacturing [1–3]. Furthermore, laser cladding can address the limitations of traditional methods such as embedding cast iron cylinder liners or thermal-spraying wear-resistant coatings on aluminum alloy surfaces. The use of martensitic stainless steel for the inner wall of the cylinder of the cast aluminum engine, prepared through rotatable inner hole laser cladding technology, offers a promising approach for improving the wear resistance of aluminum alloys [4]. This method has the advantages of low cost, high efficiency, and good wear resistance, making it an essential application for the automotive industry.

However, the fusion welding process involving steel and aluminum is challenging due to the creation of fragile intermetallic compounds (IMCs) at the joint interphase. The Fe-Al phase diagram shows that the metallurgical reactions in the weld pool lead to the creation of complicated IMCs in the joint area, which can adversely affect joint performance. The laser cladding interface presents another complication where rapid solidification leads to chaotic characterization, further derailing the interface, with the η phase and θ phase

being the most harmful due to their lower formation enthalpy [5]. According to Šlapáková et al. [6], the growth and development of these intermetallics are primarily governed by diffusion, with the kinetics of growth of the intermetallic layer following a parabolic law. To enhance the ductility continuity of the Fe-Al binary IMC layer at the joint, the introduction of alloying elements becomes necessary. Zhou et al. [7] confirmed that the average tensile–shear strength of a Si-added joint was higher than that of a Mn-added joint, owing to an improvement in the metallurgical reaction. Furthermore, the strength of both joints surpassed that of a no-added joint.

Zn serves as a vital element in joining iron and aluminum through the formation of a ternary IMC with Fe and Al. This presence of a ternary IMC can have a positive impact on the joint's properties by improving its mechanical performance, corrosion resistance, and bonding strength. Zn is commonly used as a coating material on steel surfaces to improve corrosion resistance, which is known as galvanization. According to Yan et al. [8], the addition of Zn effectively improved the interface bonding behavior. Zn is a low-melting-point element, and the IMCs formed with Al and Fe have a low melting point, which reduces the interface metallurgical reaction temperature, resulting in a process similar to instant liquid phase diffusion welding. In addition, Zn also enhances the wetting of Al on the Fe surface [9]. Peyre et al. [10] found that galvanized assemblies exhibited higher mechanical resistance than non-galvanized ones. However, the exact reason why intermetallic layers with added Zn are more shear-resistant (or more adherent) than pure Fe_2Al_5 is still under investigation. The improvement of the interface strength of η-phase-containing Zn does not have any direct evidence to be attributed to its better mechanical properties. According to Springer et al. [11], Zn has a significant effect on the metallurgical reaction rate of Fe-Al in a balanced condition, primarily the growth rate of the η phase. A more extensive and stable layer of the η phase may be the reason for improving mechanical performance. The presence of a thick Zn layer that vaporizes under laser irradiation significantly modifies the assemblies' microstructure near the interfacial zones and the failure modes, mainly located in the fusion zone.

The influence of Zn on the Fe-Al interface in Fe-Al laser cladding has not been extensively studied. Laser cladding of iron-based cladding layers on aluminum alloys involving a melting welding process can have chaotic characteristics at the interface. As described by Nguyen et al. [12], the morphology of the interface is caused by the molten material flow during the laser–powder interaction and non-repetitive formation of intermetallic layers. The degree of melting of the Al substrate is affected by both the high-temperature Fe melt and direct laser radiation. Furthermore, when high-temperature, high-density Fe powder comes into contact with the Al substrate melt pool, simultaneous metallurgical reactions and sinking occur, which results in a complex interface of the Al alloy surface laser-cladded with an Fe-based coating. As such, the role of Zn in this process requires further investigation.

DFT constitutes an integral tool in studying the mechanical and thermal properties of materials [13], and it can help reveal the effect of Zn atoms on the η phase. Currently, experimental and computational results have been able to determine the formation enthalpy and binding energy of Fe-Al IMCs [14,15]. A consistent conclusion based on the formation enthalpy of Fe-Al is that the η phase has a lower generation enthalpy and higher room temperature stability [16]. Zhang et al. [17] used the embedded-atom method (EAM) to calculate the mechanical properties of Fe-Al IMCs and found that the bulk moduli of the compounds increase with increasing Fe concentration. Li et al. [18] also computed the mechanical properties of Fe-Al IMCs and revealed that all the compounds, except for Fe_3Al and $FeAl_2$, are brittle materials. The joint's shear failure morphology displays a brittle characteristic with some localized ductile zones, which may primarily be associated with the brittle IMCs, including FeAl, Fe_2Al_5, $FeAl_3$, and Fe_4Al_{13}. However, there is a lack of research on the formation enthalpy of the η phase containing Zn, and computational results related to finite temperature are yet to be reported.

This paper aims to investigate the influence of Zn on the interface phase, microstructure, and shear resistance of the Fe-based laser cladding layer on an Al alloy surface. Through the DFT method, this study explicitly defines the mechanical performance, physical properties, and electronic distribution of Zn on the η phase interface. The findings of this study will provide both experimental and theoretical evidence to support the laser joining of an Fe-Al alloy.

2. Materials and Methods

2.1. Applied and Laser Alloying Processes of Zn Layer

Aluminum plates with a thickness of 4 mm were prepared, which featured an applied Zn powder layer and a laser alloying Zn layer. As shown in Figure 1a, secondary electron (SE) morphology demonstrates that Zn particles are spheroidal. The particle diameter (D/μm) distribution was characterized by a Mastersizer 3000E laser particle size analyzer (Malvern Panalytical, Malverncity, UK), where the particle diameter at 10% cumulative undersize is represented by a D_{10} of 3.350 μm, at 50% cumulative undersize is represented by a D_{50} of 5.406 μm, and at 90% cumulative undersize is represented by a D_{90} of 8.673 μm, as shown in Figure 1b. Zn powder was supplied by Beijing Zhongke Yannuo New Material Technology Co., Ltd., Beijing, China, and the purity was 99.9%. In contrast to the side-blowing shielding gas typically used in laser welding, the shielding gas blowing towards the substrate's surface in the laser cladding process can easily disperse. To prevent the blowout of Zn powder, which can be caused by high-flow direct protection gas, poly(vinyl alcohol) (PVA) was used as an adhesive to firmly attach the Zn powder to the substrate's surface. To prepare the adhesive, PVA powder was dispersed in anhydrous ethanol, and a 10% PVA aqueous solution was formed by pouring the PVA mixture into deionized water at 95 °C. After the PVA solution became clear, Zn powder was added and mixed into a suspension utilizing a magnetic stir bar. The amount of applied Zn powder ranged from 20 to 80 mg × cm^{-2}. The mixture was then poured onto the substrate's surface, and after drying, a high-quality Zn layer was obtained.

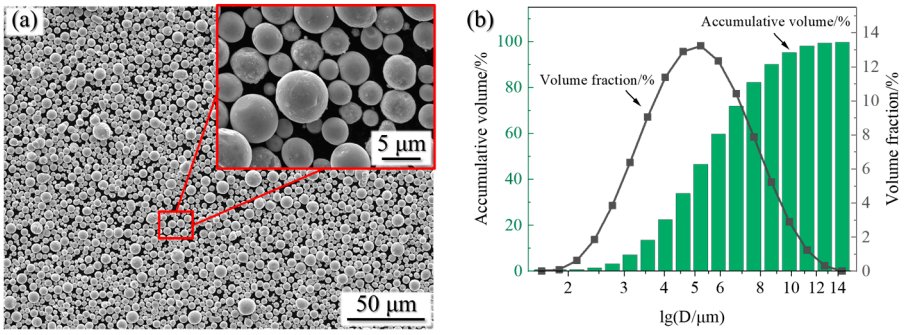


Figure 1. Characterization of Zn powders: (**a**) SE morphology and magnified view of Zn powders, and (**b**) particle diameter distribution.

Galvanized steel can be produced by either electroplating or hot plating. Similarly, two processes were proposed in this study: direct cladding with applied Zn powder layer (process 1) and alloying Zn layer (process 2). For process 2, prior to the cladding process, Zn powder was pre-scanned by a laser beam to prepare the Zn alloying layer on the Al substrate's surface. A 2500 W semiconductor laser with a 915 ± 10 nm wavelength was utilized, and its focal point had a diameter of 2 mm. Figure 2 illustrates the surface after laser scanning, revealing that the alloying Zn layer is less dense for a laser power lower than 1000 W (Figure 2a), whereas cracks appear when the laser power is 1250 W (Figure 2c). Consequently, a laser power of 1000 W was employed to produce the laser alloy Zn layer. Aluminum plates applied with 20 mg × cm^{-2} and 80 mg × cm^{-2} Zn powder were subjected to laser alloying at 1000 W, resulting in surface morphologies as shown in Figure 2b,d. The element composition of the cross-section was obtained through energy spectrum measurement of the cross-section, as shown in Table 1. The thickness of the

alloying layer was approximately 10–20 µm, with sintered Zn clusters and Al-Zn eutectic being the primary component mixture, as shown in Figure 1e,f. As the thickness of the Zn layer increased, the radius of the Zn clusters also increased.

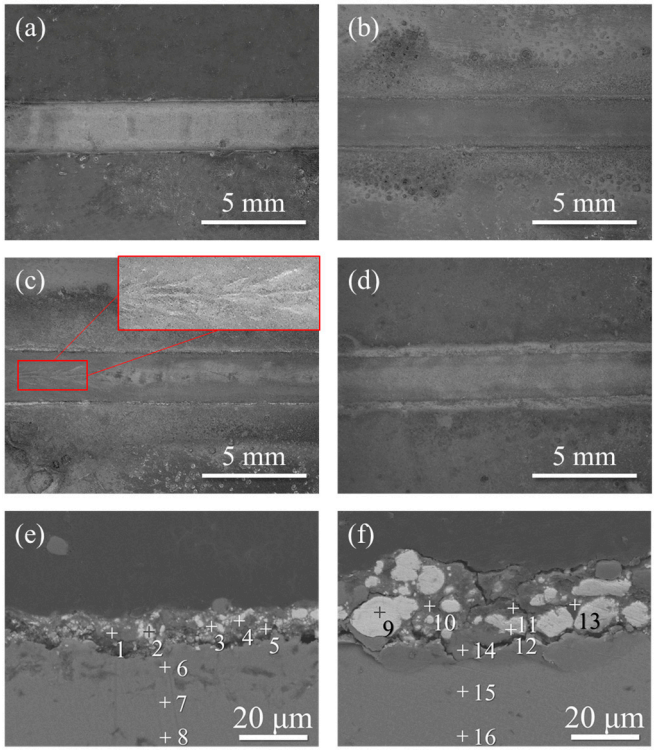


Figure 2. Surface morphology after laser alloying with varying amounts of applied Zn powder and laser powers: (**a**) 20 mg × cm^{-2} and 250 W, (**b**) 20 mg × cm^{-2} and 1000 W, (**c**) 20 mg × cm^{-2} and 1250 W with magnified view within the red boxed area revealing the presence of minute cracks, (**d**) 80 mg × cm^{-2} and 1000 W; cross-section morphologies of (**e**) 20 mg × cm^{-2} and (**f**) 80 mg × cm^{-2} applied Zn powder after laser alloying by laser power 1000 W.

Table 1. Element content of the test points, at.%.

	Point	1	2	3	4	5	6	7	8
20 mg × cm^{-2}	Al	95.67	6.20	55.97	42.23	24.71	96.54	99.26	99.57
	Zn	4.33	93.80	44.03	57.77	75.29	3.46	0.74	0.43
	Point	9	10	11	12	13	14	15	16
80 mg × cm^{-2}	Al	3.29	57.92	60.46	10.65	27.69	97.40	98.76	98.72
	Zn	96.71	42.08	39.54	89.35	72.31	2.60	1.24	1.28

2.2. Laser Cladding Method

The cladding material used in this study was 1Cr17Ni2B1Si1 martensitic stainless steel powder, which is illustrated in Figure 3a. Subsequently, the cladding experiment was carried out as depicted in the schematic diagram of Figure 3b, and the laser cladding equipment is displayed in Figure 3c. The same laser as the one mentioned in Section 2.1 was used. To ensure that the Fe-based powder was entirely melted, the laser's focus position was adjusted to adequately affect the powder flow. Additionally, the powder flow focus was placed 2 mm higher than the substrate, resulting in more thorough heating of the powder particles. The specific cladding parameters are available in Table 2.

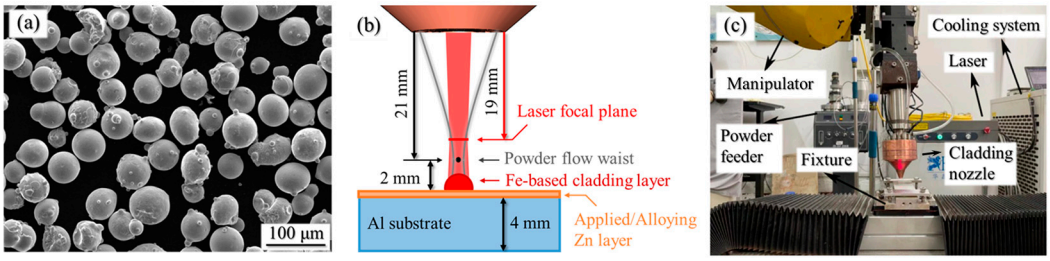


Figure 3. Laser cladding material and process: (**a**) SE morphology of 1Cr17Ni2B1Si1 martensitic stainless steel powder, (**b**) schematic of laser cladding process and (**c**) laser cladding equipment.

Table 2. Cladding parameters.

Parameter	Unit	Value
Laser power	W	2000
Cladding speed	$m \times min^{-1}$	1.0
Carrier gas pressure	MPa	0.1
Carrier gas flow rate	$L \times min^{-1}$	8.0
Powder feeding rate	$g \times min^{-1}$	28.8
Shielding gas pressure	MPa	0.2
Shielding gas flow rate	$m^3 \times h^{-1}$	1.0

2.3. Phase Characterization and Shear Test

The samples were polished using a diamond polishing compound after being polished to a 2000 grit size emery paper. Keller reagent was employed to corrode it until the interface between the cladding layer and the substrate became apparent. To investigate the interface characteristics, scanning electron microscopy (SEM; TESCAN MIRA3, TESCAN, Brno, Czech Republic) was used to examine the cross-sectional microstructures. The composition distribution at the interface was analyzed using the equipped backscattered electron (BSE, TESCAN, Brno, Czech Republic) and energy dispersive spectroscopy (EDS, TESCAN, Brno, Czech Republic) probes. In Figure 4, the interface shear resistance strength is determined by measuring the shear force of the cladding layer, which is then divided by the area of the section to calculate the shear stress. The phase of the fracture surface was tested using an X'Pert PRO X-ray diffractometer (Malvern Panalytical, Malverncity, UK).

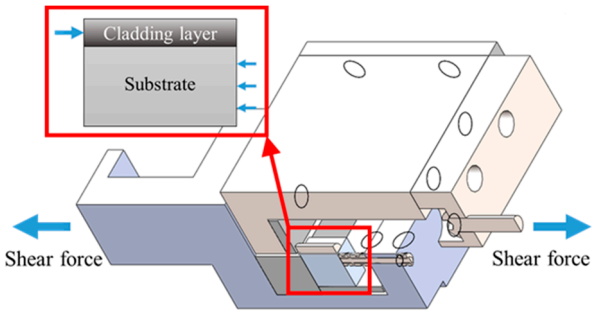


Figure 4. Shear fixture diagram and test process.

2.4. DFT Calculation

We used the Vienna Ab initio Simulation Package (VASP) to perform the first principle calculation of Fe_2Al_5 and $Fe_2Al_5Zn_x$ based on the density functional theory (DFT) [19–21]. The generalized gradient approximation (GGA) and projected affixed wave (PAW) methods proposed by Perdew, Burke and Ernzerhof (PBE) were used to evaluate the exchange correlation energy [22]. By using the method proposed by Monkhost-Pack, the energy integral was characterized as the first irreducible Brillouin zone [23]. For Fe_2Al_5 and $Fe_2Al_5Zn_x$ crystal cells, the grid size was $7 \times 8 \times 11$. The maximum energy cut-off value

was used for plane wave expansion in reciprocating space, and the value was 500 eV. During the optimization process, the change of total energy converged to 10^{-5} eV.

Using the stress–strain method and generalized Hooker's law, we computed the elastic constants for Fe_2Al_5 and $Fe_2Al_5Zn_x$. We employed various strain patterns to determine the crystal structure and assessed the Cauchy stress tensor for each mode of strain. The elastic constants were then derived from the strain–stress relationships described in Equation (1):

$$\begin{pmatrix} \sigma_1 \\ \sigma_2 \\ \sigma_3 \\ \tau_4 \\ \tau_5 \\ \tau_6 \end{pmatrix} = \begin{pmatrix} C_{11} & C_{12} & C_{13} & C_{14} & C_{15} & C_{16} \\ C_{21} & C_{22} & C_{23} & C_{24} & C_{25} & C_{26} \\ C_{31} & C_{32} & C_{33} & C_{34} & C_{35} & C_{36} \\ C_{41} & C_{42} & C_{43} & C_{44} & C_{45} & C_{46} \\ C_{51} & C_{52} & C_{53} & C_{54} & C_{55} & C_{56} \\ C_{61} & C_{62} & C_{63} & C_{64} & C_{65} & C_{66} \end{pmatrix} \begin{pmatrix} \varepsilon_1 \\ \varepsilon_2 \\ \varepsilon_3 \\ \gamma_4 \\ \gamma_5 \\ \gamma_6 \end{pmatrix} \quad (1)$$

where σ_i is normal stress, τ_i is the shear stress, C_{ij} is the elastic constant, γ_i is the shear strain and ε_i is the corresponding normal strain. Anisotropic elastic properties were created by running the elastic anisotropy measures (ElAM) code [24].

3. Results and Discussion

3.1. Cross-Section of the Cladding Layer

Figure 5 illustrates the cross-section of the cladding layer, the thickness measurement results of the cladding layer, and its contact angle with the substrate. The reference line is the substrate surface, and the contact angle is the angle between the cladding layer's surface at the weld toe and the reference line. The thickness is the vertical length from the peak of the cladding layer to the reference line.

In process 1, the thickness of the cladding layer shows a tendency to decrease as the amount of applied Zn powder increases, as shown in Figure 5i. However, there may be a degree of randomness in the measurement outcomes, as evidenced by the slightly lower values of 564 μm and 592 μm. Conversely, in process 2, the thickness of the cladding layer increases, and there is no consistent change in thickness between the two processes. The heat absorbed during the melting of the Zn powder in process 1 causes the substrate temperature to decrease, which results in reduced efficiency in Fe-based cladding deposition and a subsequent decrease in the thickness of the cladding layer. In process 2, there is little correlation between the amount of applied Zn powder layer and the powder deposition efficiency. The thickness of the cladding layer is determined by its spreading when the contact angle of the Fe-based cladding layer is small and is restricted by surface tension [9]. This leads to an increase in the thickness of the cladding layer.

As the amount of applied Zn powder layer increases, the contact angle of the cladding layer decreases; process 1 shows a greater reduction than process 2, as shown in Figure 5j. This is because Zn is attached to the surface of the Al substrate in a solid state, and it absorbs a significant amount of heat from the Fe droplet, causing it to solidify before it spreads completely. An alloying Zn layer forms a surface agglomeration, making it easier to spread the liquid Fe-based droplet.

3.2. Interface Element Content and Phase Distribution

3.2.1. Interface of Process 1 (Applied Zn Powder Layer)

Figure 6 shows that with an increase in the amount of Zn powder, the local η phase thickens, with a maximum thickness of 29.3 μm and a minimum thickness of 1.6 μm. The η phase thickens with an increase in Zn content. Springer et al. [11] attributed this phenomenon to the improved growth kinetics of the η phase from Zn. Moreover, an increase in applied Zn powder causes an enhancement of the interface discontinuity. Figure 6c,d demonstrate a significant deposition of particles into the Al substrate.

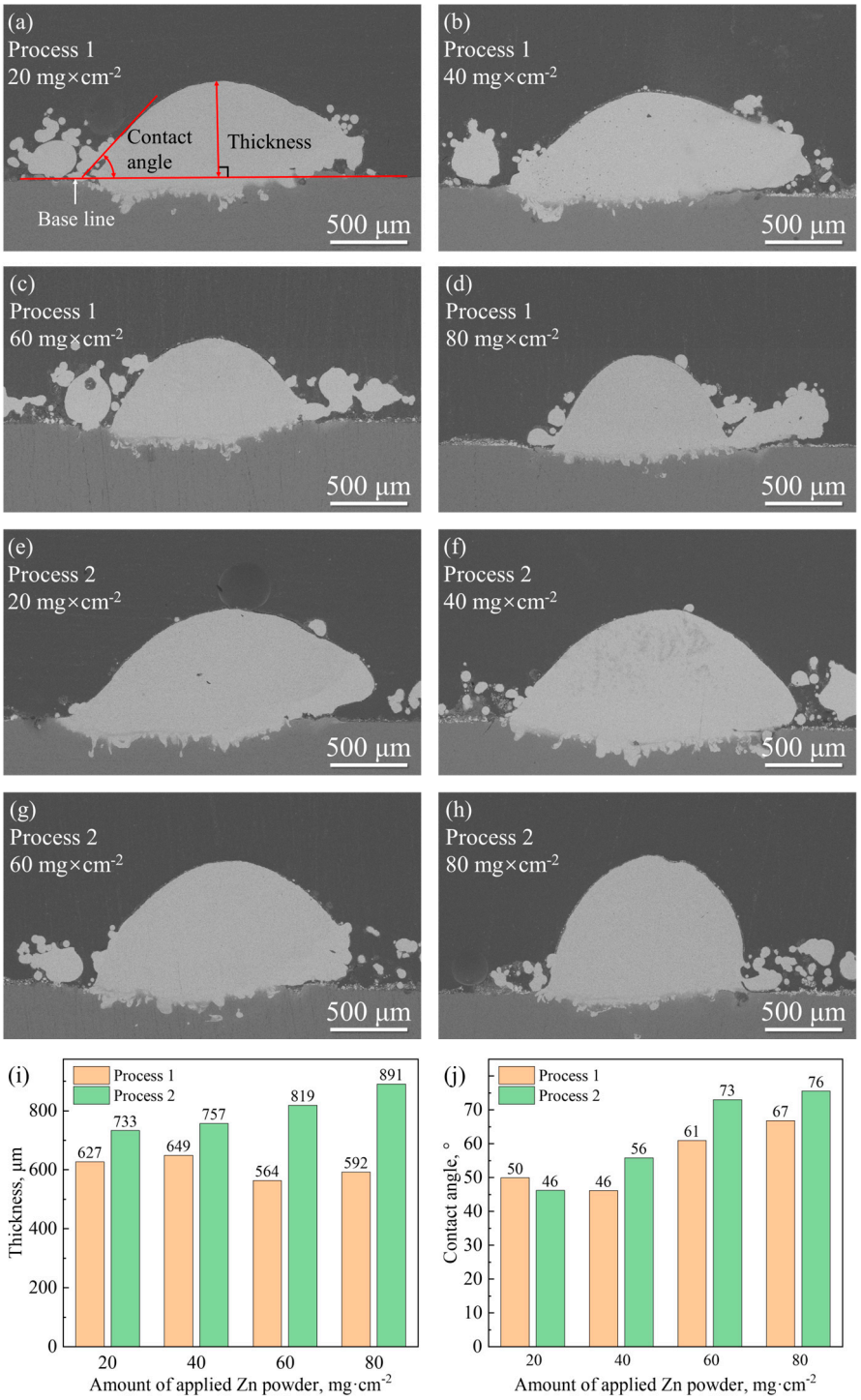


Figure 5. The (**a**–**h**) BSE morphologies, (**i**) thickness and (**j**) contact angle of the cross-section of the cladding layer. The red lines and arrows indicate the measurement methods for the thickness of the cladding layer and the contact angle.

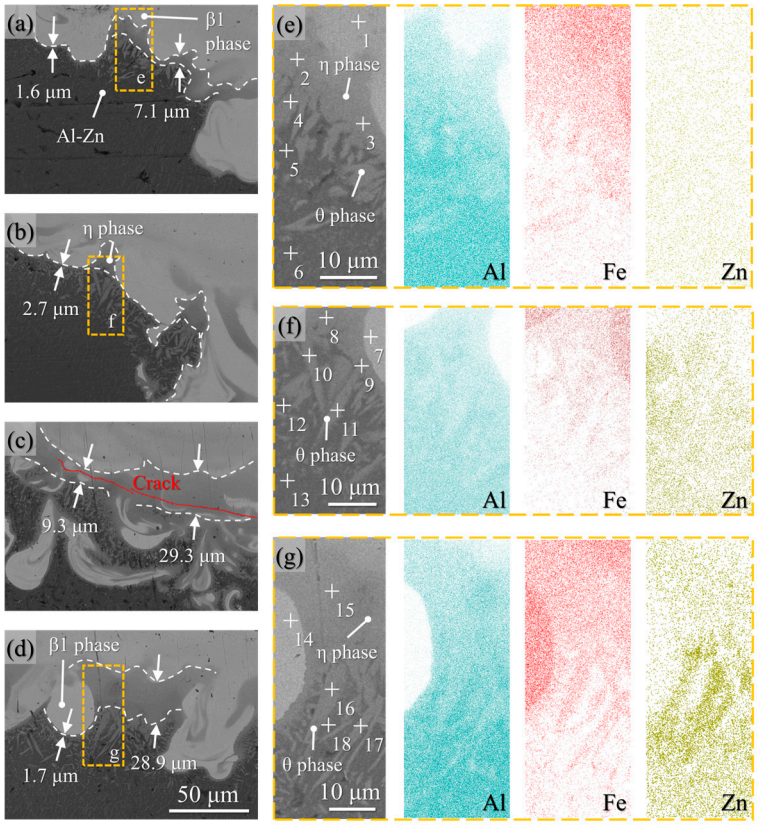


Figure 6. BSE morphologies of interface with applied Zn powder (**a**) 20 mg × cm^{-2}, (**b**) 40 mg × cm^{-2}, (**c**) 60 mg × cm^{-2}, (**d**) 80 mg × cm^{-2}; and magnified segments showing element distribution of specific areas from (**a**,**b**,**d**) corresponding to (**e**–**g**), respectively.

Figure 6e–g illustrate that a greater amount of applied Zn powder changes the θ phase on the near Al side from a pinkish needle to a lath. At the same time, there are distinct differences in the distribution of Zn at the interface. This difference is not observed in Figure 6e when the Zn content is low, but it is evident in Figure 6f,g as the Zn content increases. Firstly, compared to IMC phases, Zn significantly enriches the Al substrate, as demonstrated in Table 3 with a 40 mg × cm^{-2} concentration of Zn. The Zn content in the substrate is approximately 2.43%, which is higher than the concentrations observed in the η and θ phases (1.50% and 1.29%, respectively). Secondly, in different substrate regions, Zn manifests component segregation, as illustrated by Figure 6g.

Zn is concentrated in the Al substrate in the dendrite gap of the θ phase, indicating that Zn has a high affinity for the substrate. In conclusion, the Zn content in the θ phase is approximately 0.59% to 0.87%, and exceeds 2.77% in the η phase, as shown in Table 3.

3.2.2. Interface of Process 2 (Alloying Zn Layer)

As illustrated in Figure 7, an increase in Zn content resulted in the thickening of the η phase at the interface from approximately 9.6 μm to 43.6 μm and the coarsening of dendritic microstructure width adjacent to the aluminum interface from 1 μm to 5 μm. Energy spectrum testing at points 3 and 9 in Table 4 revealed that the dendritic microstructure's primary component is the θ phase, with 80% aluminum content. Furthermore, differences exist in the distribution of Zn at the interface, akin to the process seen in Figure 6. Table 4 shows that the substrate's Zn content ranges from 3.60% to 5.15%, higher than those found in the η and θ phases (2.56% and 1.48%, respectively). Consequently, Zn is significantly enriched in the aluminum substrate. According to Table 4, the Zn content in the θ phase is about 1.48% and 2.56% in the η phase.

Table 3. Element content at the test point of process 1, at.%.

Process	Position	Al	Cr	Fe	Zn	Phase
20 mg × cm^{-2}	1	16.30	13.32	70.39	0	β1-$(Fe\text{-}Cr)_3Al$
	2	70.80	3.58	25.18	0.45	η-$(Fe\text{-}Cr)_2Al_5Zn_x$
	3	69.13	7.78	22.49	0.61	η-$(Fe\text{-}Cr)_2Al_5Zn_x$
	4	81.89	1.19	16.26	0.65	θ-$(Fe\text{-}Cr)_4Al_{13}$
	5	98.55	0.07	0.66	0.72	Al-Zn
	6	97.74	0.35	1.55	0.36	Al-Zn
40 mg × cm^{-2}	7	2.46	16.10	80.41	1.03	M-Fe_4Cr
	8	71.63	4.53	22.34	1.50	η-$(Fe\text{-}Cr)_2Al_5Zn_x$
	9	71.06	4.89	22.93	1.12	η-$(Fe\text{-}Cr)_2Al_5Zn_x$
	10	78.95	1.40	18.37	1.29	θ-$(Fe\text{-}Cr)_4Al_{13}$
	11	79.69	1.95	17.32	1.05	θ-$(Fe\text{-}Cr)_4Al_{13}$
	12	93.50	0.11	0.65	5.74	Al-Zn
	13	95.72	0.55	1.31	2.43	Al-Zn
80 mg × cm^{-2}	14	10.16	19.38	70.16	0.29	M-Fe_4Cr
	15	63.78	4.85	28.60	2.77	η-$(Fe\text{-}Cr)_2Al_5Zn_x$
	16	77.74	2.02	19.66	0.59	θ-$(Fe\text{-}Cr)_4Al_{13}$
	17	80.35	1.78	17.00	0.87	θ-$(Fe\text{-}Cr)_4Al_{13}$
	18	92.44	1.06	1.41	5.09	Al-Zn

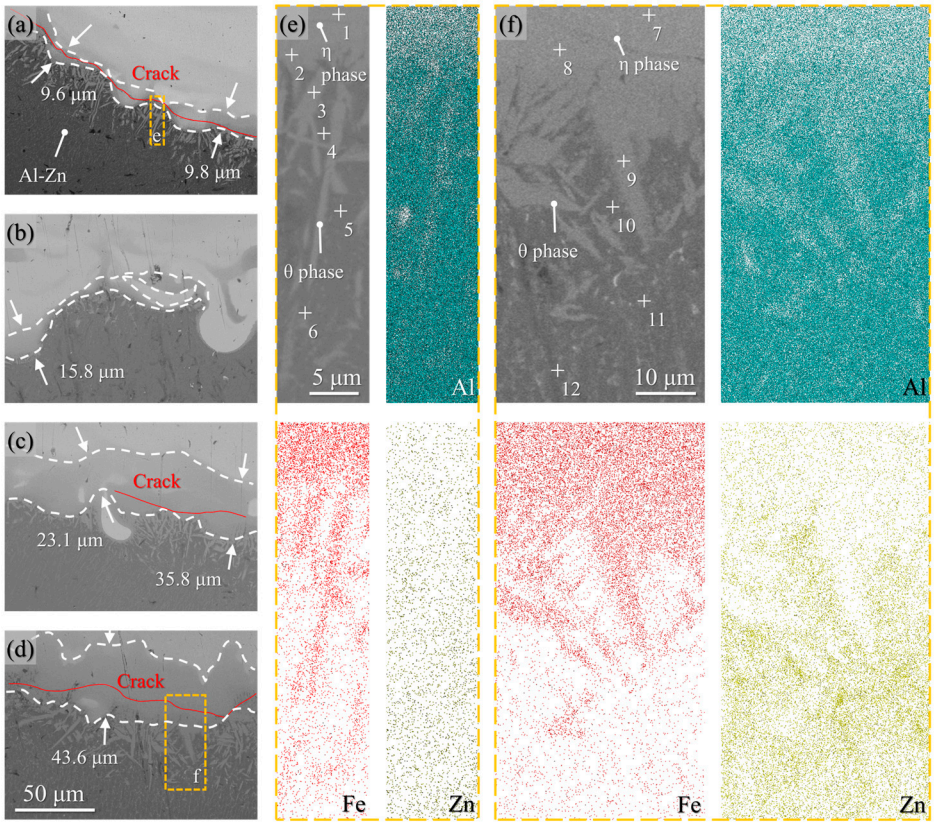


Figure 7. BSE morphologies of interface with applied Zn powder (**a**) 20 mg × cm^{-2}, (**b**) 40 mg × cm^{-2}, (**c**) 60 mg × cm^{-2}, (**d**) 80 mg × cm^{-2}; and magnified segments showing element distribution of specific areas from (**a**,**d**) corresponding to (**e**,**f**), respectively.

Table 4. Element content at the test point of process 2, at.%.

Process	Position	Al	Cr	Fe	Zn	Phase
40 mg × cm^{-2}	1	67.48	6.11	25.81	0.59	η-$(Fe\text{-}Cr)_2Al_5Zn_x$
	2	69.49	4.71	24.91	0.88	η-$(Fe\text{-}Cr)_2Al_5Zn_x$
	3	81.66	2.96	14.79	0.59	θ-$(Fe\text{-}Cr)_4Al_{13}$
	4	93.90	0.92	4.29	0.89	Al-Fe
	5	97.79	0.24	1.09	0.88	Al-Zn
	6	97.81	0.44	1.25	0.50	Al-Zn
80 mg × cm^{-2}	7	69.10	2.97	25.37	2.56	η-$(Fe_4Cr)_2Al_5Zn_x$
	8	70.03	6.09	20.92	2.96	η-$(Fe_4Cr)_2Al_5Zn_x$
	9	80.52	2.39	15.60	1.48	θ-$(Fe_4Cr)_4Al_{13}$
	10	94.38	0.38	1.31	3.93	Al-Zn
	11	94.51	0.14	0.20	5.15	Al-Zn
	12	94.97	0.21	1.22	3.60	Al-Zn

During both processes, a chaotic interface was formed when a larger Fe droplet entered the substrate. However, this droplet fails to diffuse and react fully, quickly solidifying and forming a bonding interface that has chaotic characteristics.

Process 1 and process 2 show a discrepancy in that Zn powders in process 1 absorb heat during cladding to shorten reaction time and reduce reaction temperature compared to process 2. This results in a thinner η phase layer and a shorter time for dendrite nucleation of the θ phase to grow, illustrated by the formation of a short rod-shaped θ phase in Figure 7e. The content of Zn in process 1 is slightly higher than in process 2 at the interface, indicating Zn diffusion during laser alloying. However, this may lead to a certain amount of burning loss, as evidenced in Table 1.

Figures 6c and 7a,c,d demonstrate the microcracks at the interface, particularly along the red line position. These cracks penetrate the η phase and are adjacent to the side of the aluminum substrate due to the higher aluminum content in the IMC interface adjacent to the aluminum side. Aluminum-rich intermetallics exhibit high brittleness. The composition assessment in Table 4 shows that the Al content of the IMC near the crack is about 70%, indicating an η phase. Discontinuous microcracks can also be observed at the η layer, which may lead to a reduction in the contact area of the cladding layer and a reduced interface bonding strength. However, subsequent tensile tests showed no significant correlation between microcracks and the shear strength of the cladding layer.

Zn is enriched in the substrate. There are two possible reasons for this: (1) The melting point of the Al substrate is lower than that of Fe, allowing the liquid to last longer after being acted upon by the molten Fe. This is conducive to Zn diffusion in the Al substrate. (2) The solid solubility of Zn in Al is high. The uneven distribution of Zn in the Al substrate is mainly due to the difference in temperature of the Fe droplets.

Although the θ phase and η phase undergo solid–liquid transformation at nearly the same time (their respective melting points, 1160 °C and 1166 °C, respectively, are similar [25]), the content of Zn in the two phases is distinct. This is because the [001] direction of the η phase encourages the diffusion of Zn atoms, leading to Zn atoms' rapid diffusion in the η phase even in the solid state at high temperatures [26].

3.2.3. Effect of Zn Content and Surface Energy Density on η Phase Thickness

Figure 8 illustrates the relationship between the thickness of the η phase layer and the amount of applied Zn powder in the two processes. Process 1 results in the thickest η phase layer at the bonding interface when the amount of Zn powder applied reaches 60 mg × cm^{-2}. On the other hand, process 2 exhibits a gradual thickening of the η phase layer with increasing amounts of Zn powder applied. Generally, Zn increases the thickness of the η phase layer significantly, whereas laser alloying the Zn layer can stabilize the thickness fluctuation of the η phase layer, as shown by the small error bar.

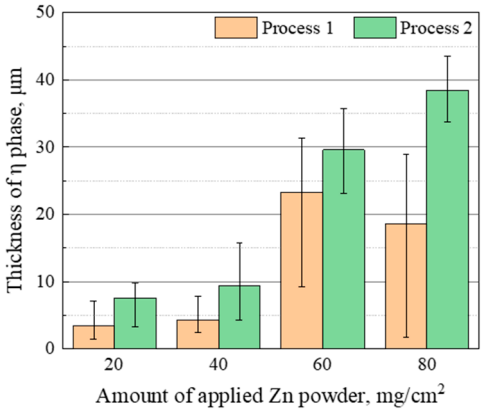


Figure 8. Comparison of the thickness of the η layer under two different processes at various amounts of applied Zn powder.

Springer et al. [11] suggests that under constant temperature conditions, the Zn layer enhances the reaction kinetics of the η phase. There may be no change in activation energy, but an interaction of Zn with the structural vacancies of the η phase likely causes its accelerated growth. Applying Zn coatings onto steel is advantageous for solid–liquid joining procedures, assisting bonding by enabling rapid dissolution and forming even and ordered reaction layers [27]. Laser cladding exhibits non-equilibrium metallurgical reactions. Based on the above results, there is a positive correlation between the growth thickness of the η phase and Zn at the interface. Ternary compounds of Zn, Fe, and Al have lower melting points. Thus, under the same temperature cycle, the lower the melting point, the longer the liquid duration, leading to continued Zn consumption within the reaction. Consequently, higher Zn content prolongs the reaction duration.

Various processes and material brands significantly influence the thickness of the η phase layer at the interface of a Fe-Al laser joint. Table 5 summarizes the Zn layer thickness (T_{Zn}), η phase thickness (T_η), velocity (v), laser power (P), laser spot diameter (d), and material brand of different Fe-Al laser joining technologies.

Suder et al. [34] proposed a definition of specific point energy to analyze the effects of welding parameters and processes. However, the formula's applicability is restricted to small beam diameters, requiring a laser beam with uniform intensity distribution and constant interaction time across the laser spot. When investigating the influence of altered laser power density, the impact of spot diameter on power density is negatively correlated. On the basis of the linear energy density described by Yang et al. [5], we divided it by the equivalent spot diameter of the laser spot to produce the area energy density. By analyzing the relationship between surface energy density and η phase thickness, the relationship is determined using the surface energy density expressed as Equation (2):

$$\rho = \frac{P}{vd} \tag{2}$$

where ρ is surface energy density, P is laser power, v is welding velocity, and d is laser spot diameter.

Figure 9 summarizes and compares the impacts of surface energy density and the Zn coating on the thickness of the η phase at the interface. The thickness of the η phase is influenced by both the presence of Zn at the interface and the surface energy density. A higher surface energy density clearly increases the thickness of the η phase at the interface. Under the same surface energy density, a Zn layer attached to the surface before processing significantly boosts the thickness of the η phase at the interface, exemplified by the results of Ogura et al. [30], who imposed a 7.1 μm Zn layer. However, Al-1.88Si wire is used for wire filling connection where Si inhibits the growth of the η phase. The results of Rathod et al. [28] adopted the rolling method, resulting in the formation of a thicker η layer despite the absence of Zn addition. Notably, Ozaki et al. [33] adopted a similar method to

Rathod et al. [28]. Still, the η layer formed under the same surface energy density is thinner when compared to Rathod. This may be due to the different distance between the laser center and the contact point of the roller (17 mm [28] vs. 25 mm [33]).

Table 5. Zn layer thickness (T_{Zn}), thickness of η phase ($T_η$), velocity (v), laser power (P), laser spot diameter (d), materials brand of some Fe-Al laser joining technologies.

Initial Surface	T_{Zn}, μm	$T_η$, μm	v, mm×s^{-1}	P, W	d, mm	Materials Brand	Ref.
Without Zn coating	0	4 5 8	20 16.7 11.7	3000	1	6016/DC 04	[10]
		10 2	25 40	1500	2.5–3.5	5052/low carbon steel	[28]
		5 3 1	10 10 10	2200	0.85	6061/S235-JR	[29]
Zn coated	10	23 8 4	10 20 23.3	3000	1	6016/DC 04	[10]
	7.1	30 3	5 3.33	1500	1.5	A5052/SPCC-GA	[30]
	20	40 5	10 23.3	3000	~2	6016/DC 04	[31]
	10	5 9 12	11.7 11.7 11.7	1000 1300 1600	2 × 0.8	7075/DP590	[32]
	20	3.5 1.2	8.3 10	1500	~1.5	GI/A6000	[33]

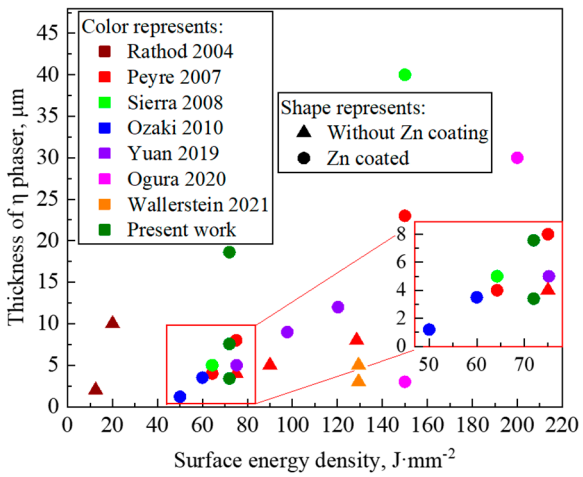


Figure 9. Impact of surface energy density and Zn coating on η phase thickness at interface [10,28–33].

3.3. Shear Resistance

3.3.1. Shear Strength and Fracture Analysis

The information shown in Figure 10 indicates that the amount of applied Zn powder has a noteworthy impact on the shear strength of the cladding layer. Initially, the shear strength of the cladding layer increases with the rise in the amount of Zn powder up to a particular point, then it begins to decrease.

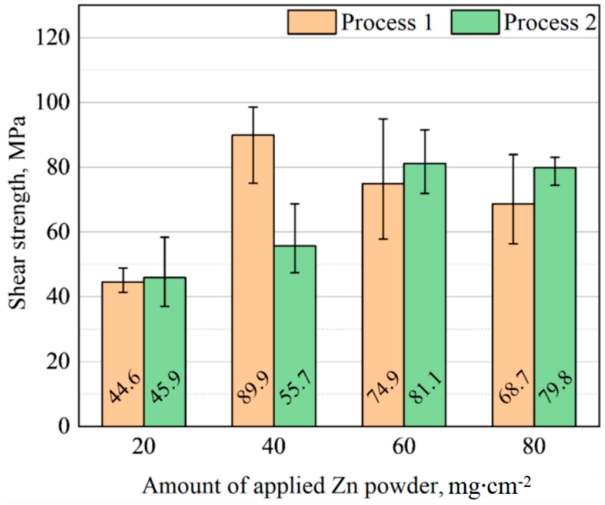


Figure 10. Shear strength of the interface.

Process 1 resulted in the highest shear strength of the cladding layer at 40 mg × cm^{-2} of applied Zn powder, which was 89.9 MPa. On the other hand, the greatest average shear strength of the cladding layer for process 2 was produced by the implementation of 60 mg × cm^{-2} of Zn powder, which resulted in 81.19 MPa. However, the cladding layer's maximum shear strength slightly decreases when the amount of applied Zn powder increases to 80 mg × cm^{-2}, but the standard deviation decreases, indicating more stable shear resistance. Therefore, the recommended applied Zn powder quantities can vary depending on the process used, and it should be meticulously adjusted to gain the desired shear strength and stability.

Xia et al. [35] observed that cross dual laser beams generated satisfactory weld formation and the most homogeneity of τ_5, thus resulting in joints with improved tensile strength compared to single laser beams and in-line dual laser beams. Ozaki et al. [33] discovered that specimen failure happens at the base metal, which was made through laser roll welding with a 150 MPa roll pressure.

Figure 11 shows the XRD results and macroscopic morphology of the shear fracture. As shown in Figure 11a, the shear fracture zone consists mainly of the Al phase, the $Fe_2Al_5Zn_x$ phase, the Fe_4Al_{13} phase, and a small quantity of the Zn phase. This composition is consistent with the EDS analysis results mentioned above. The composition of the shear fracture surface is mainly composed of Al-riched IMCs and the Al phase, indicating that the fracture occurred at the IMCs layer, and due to the peeling effect, part of the aluminum substrate is exposed.

The shear process creates shear stress, which exposes the Al substrate in the right fracture zone. Figure 11b,c show that for process 1, when the amount of Zn powder is 20 mg × cm^{-2}, there is a point peeling area, which mainly comes from the separation of the droplet part connected with the cladding layer and the substrate together with the cladding layer. When the amount of Zn increases to 80 mg × cm^{-2}, it is mainly valley tearing.

Figure 11d,e show that for process 2, when the amount of Zn powder is 20 mg × cm^{-2}, there is not only a point peeling area, but also a valley tearing at the right part, and with the increase in the amount of applied Zn powder, the valley tear is more obvious, indicating that the shear strength of the interface is closer to the shear strength of the substrate. In addition, the flatter and more uniform bonding interface also reduces the area of the spot peeling area.

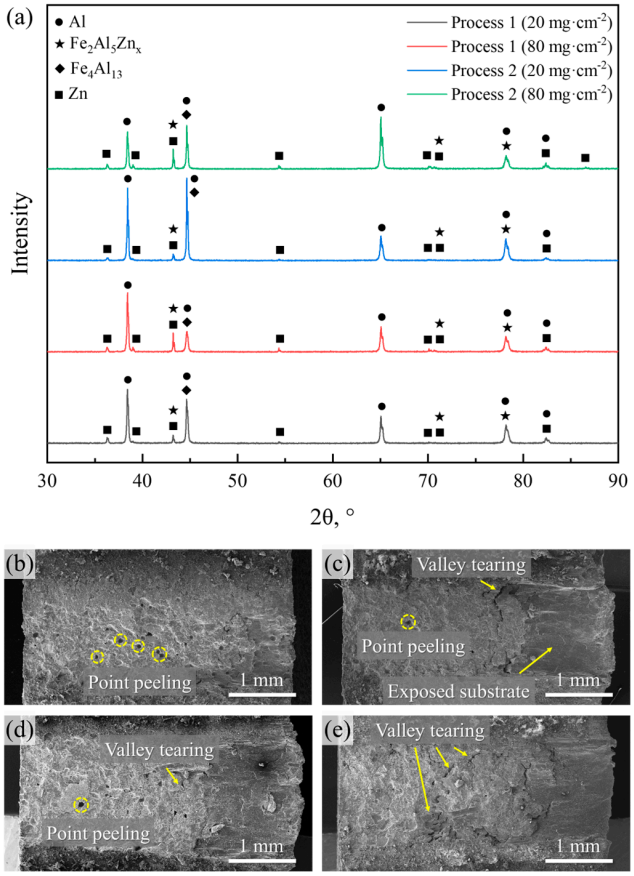


Figure 11. Shear fracture analysis of samples: (**a**) XRD results and macroscopic morphology of (**b**) process 1 with 20 mg × cm^{-2} applied Zn powder layer; (**c**) process 1 with 80 mg × cm^{-2} applied Zn powder layer; (**d**) process 2 with 20 mg × cm^{-2} applied Zn powder layer; (**e**) process 2 with 80 mg × cm^{-2} applied Zn powder layer.

3.3.2. Shear Section of Process 1 (Applied Zn Powder Layer)

Figure 12 shows the BSE and SE morphologies of the fracture section morphology with 20 mg × cm^{-2} and 40 mg × cm^{-2} applied Zn powder. The average shear strength is 44.6 MPa for 20 mg × cm^{-2} and 89.9 MPa for 40 mg × cm^{-2} applied Zn powder amounts, respectively. Table 6 shows the element content at the corresponding position in Figure 12.

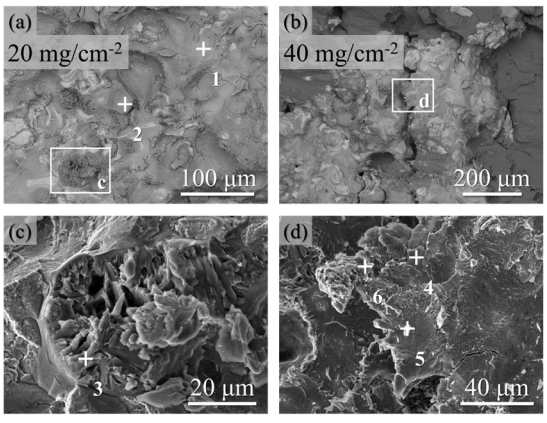


Figure 12. Fracture section morphologies of process 1: (**a**) BSE morphology with 20 mg × cm^{-2} applied Zn powder; (**b**) BSE morphology with 40 mg × cm^{-2} applied Zn powder; (**c**) SE morphology of coarse dendrites θ phase; (**d**) SE morphology of tear area.

Table 6. Element content at the corresponding position of process 1, at.%.

Process	0	Al	Cr	Fe	Zn	Phase
20 mg × cm^{-2}	1	61.75	7.31	30.11	0.84	η-$(Fe\text{-}Cr)_2Al_5Zn_{0.1}$
	2	77.13	3.4	19.27	0.19	θ-$(Fe\text{-}Cr)_4Al_{13}$
	3	84.17	3.48	11.94	0.40	θ-$(Fe\text{-}Cr)_4Al_{13}$
40 mg × cm^{-2}	4	43.94	8.79	45.88	0.39	β2-(Fe-Cr)Al
	5	66.01	5.97	25.57	2.45	η-$(Fe\text{-}Cr)_2Al_5Zn_{0.2}$
	6	78.58	2.38	19.04	0	θ-$(Fe\text{-}Cr)_4Al_{13}$

According to the composition of the sample with an applied Zn powder of 20 mg × cm^{-2}, the η and θ phases mainly exist in the section. As shown in Figure 12c, the θ phase with 84.17% Al content is at point 3, which remains on the surface of the substrate in the form of coarse dendrites. Due to the small amount of Zn, it has little effect on the formation of the Zn-rich η phase, and there is a large θ phase area.

Figure 12b shows that the sample section with an applied Zn powder of 40 mg × cm^{-2} has a long tear area. As shown in Figure 12d, the crack initiation site (point 6) of the tear area is θ phase, and the rest (point 4 and point 5) are mainly β2 and η phases, and the fracture surface presented brittle fracture. The interface strength is improved due to the higher Zn content at the interface.

With the further increase in the applied Zn powder amount reaching up to 60 mg × cm^{-2} and 80 mg × cm^{-2}, η and θ exist at the same time, mainly due to the better mechanical properties of the η phase, and its better strength. However, the discontinuity of the interface is improved and microcracks appear, as shown in Figure 6, which results in the average shear strength of the interface being lower than that of 40 mg × cm^{-2} applied Zn powder amount, but it is still higher than that of the 20 mg × cm^{-2} applied Zn powder amount.

3.3.3. Shear Section of Process 2 (Alloying Zn Layer)

Figure 13 shows the BSE and SE morphologies of the fracture section morphology with an applied Zn powder amount of 20 mg × cm^{-2} and 80 mg × cm^{-2}, yielding an average shear strength of 45.7 MPa and 79.8 MPa, respectively. Table 7 shows the element content at the corresponding position in Figure 13.

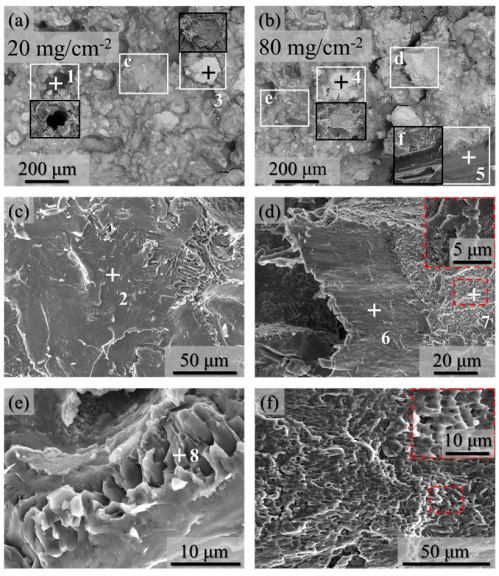


Figure 13. Fracture section morphologies of process 2: (**a**) BSE morphology with 20 mg × cm^{-2} applied Zn powder; (**b**) BSE morphology with 80 mg × cm^{-2} applied Zn powder; (**c**) SE morphology of brittle fracture; (**d**) SE morphology of tear area; (**e**) SE morphology of coarse dendrite θ phase; (**f**) SE morphology of torn Al substrate area.

Table 7. Element content at the corresponding position of process 2, at.%.

Process	Point	Al	Cr	Fe	Zn	Phase
20 mg × cm^{-2}	1	97.25	0.05	2.62	0.98	Al-Fe-Zn
	2	61.67	6.17	31.48	0.68	η-$(Fe\text{-}Cr)_2Al_5$
	3	12.05	16.17	71.03	0.75	α-(Fe-Cr)
80 mg × cm^{-2}	4	5.97	18.58	75.37	0.09	α-(Fe-Cr)
	5	97.61	0.08	0.74	1.58	Al-Fe-Zn
	6	55.77	6.70	32.70	4.83	η-$(Fe\text{-}Cr)_2Al_5Zn_x$
	7	0.81	20.07	78.53	0.59	α-(Fe-Cr)
	8	77.09	2.85	18.97	1.08	θ-$(Fe\text{-}Cr)_4Al_{13}$

In Figure 13a, there is a point peeling section in area 1, and the droplet part connected with the cladding layer is separated from the substrate along with the cladding layer. According to the composition scanning in Table 7, it is found that the point peeling section is mainly composed of the Al substrate. As shown in Figure 13f, the completely torn area exposes the Al substrate, showing dense dimple morphology. In area 5 shown in Figure 13b, friction marks formed on the surface of the Al substrate due to ploughing are found.

Figure 13c displays the region on the fracture surface where the η phase is situated with an applied Zn powder of 20 mg × cm^{-2}. The fracture surface is relatively flat and presents a typical brittle fracture morphology. As shown in Figure 13d, the fracture surface with 80 mg × cm^{-2} applied Zn powder has a horizontal tear area, such as the valley area in Figure 11 above. The content of Zn in the upper part of the initial crack zone of the tear zone is 4.83% higher than that in other areas (area 6). The Al substrate also cracked under the pulling action of the Zn-rich η phase and the alpha phase during the shear test. Meanwhile, the right side of this area is the α phase, and its fracture surface is ductile. Figure 13e shows a short rod-shaped fracture structure, and its main component is θ-$(Fe\text{-}Cr)_4Al_{13}$ with high Zn content, which is derived from the residue on the substrate after the fracture of the coarse dendrite θ phase shown in Figure 7.

Under different amounts of Zn powder preform, the shear fracture surface contains two types of fracture areas with brittle and ductile fracture characteristics. The brittle fracture zone presents a fluvial pattern, as shown in the area near point 2 in Figure 13, which is mainly an exposed η phase (area 2 and area 6). The ductile fracture area is characterized by dimples. The main components of the ductile fracture zone are alpha-Fe4Cr and Al substrate areas rich in Fe and Cr, such as the areas near points 3, 4, 5, and 7. The area near point 8, which is dominated by the θ phase, presents irregular fracture morphology, and its essence is a brittle fracture.

3.4. DFT Calculation of Fe_2Al_5 and $Fe_2Al_5Zn_x$

3.4.1. Calculation Model

Figure 14 shows the crystal structure of η-Fe_2Al_5, which belongs to the orthorhombic crystal system. The space group is Cmcm (No. 63) and the lattice constant a = 7.6559 (8), b = 6.4154 (6), and c =4.2184 (4) Å. The crystal structure of Fe_2Al_5 is homologous with that of $MnAl_6$ and Co_2Al_5. When optimizing the structure of the Fe_2Al_5 crystal, Burkhardt et al. [26] pointed out that the model of the Al atom at position 4 (b) (occupied by the Al2 atom) cannot explain the continuous overlapping small peaks of electron density near y = 0.5 on the (100) crystal plane. This phenomenon can be reasonably described by adding at least one Al atom (Al3) at the position of 8 (f). Among them, the occupation factor of the Al2 atom is 0.36, and that of the Al3 atom is 0.23, as shown in Figure 14a.

Due to the interaction between Fe atoms and Al1 atoms, the Al2 and Al3 atoms in the [001] direction form a disordered distribution. As shown in Figure 14b, after the Al2 and Al3 atoms are ignored, an octagonal channel structure (or pentagonal antiprism shape) is formed in the [001] direction. The Al2 atom and Al3 atom are in the same cell and generally do not appear at the same time [26]. The reason for the emergence of channels of disordered

or incommensurately spaced atoms can be explained by the combination of preferred electron counts tied to stoichiometry and continuous paths of CP quadrupoles [36].

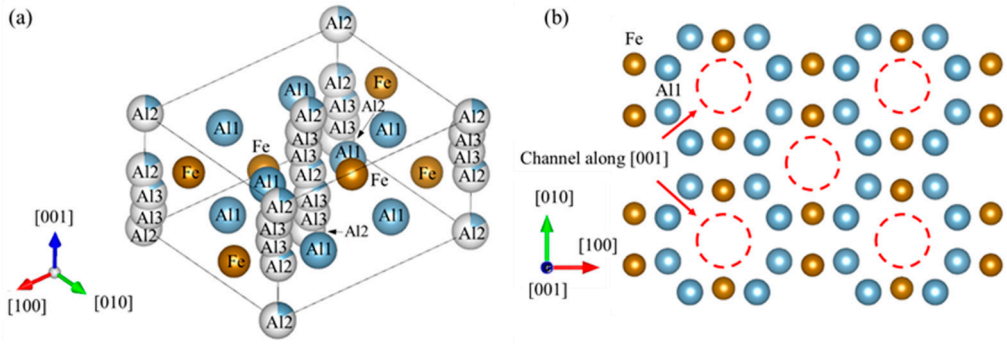


Figure 14. Crystal structure of η-Fe_2Al_5: (**a**) Atom position of Fe, Al1, Al2 and Al3, and (**b**) channel in [001] direction.

The adopted η-Fe_2Al_5 crystal structure model is shown in Figure 15a, and the aluminum atom at the Al3 position is omitted from its crystal structure. Figure 15b shows the crystal structure model of η-$Fe_2Al_5Zn_x$. In the crystal structure model, the content of Zn is close to 0.4%, and Zn atoms are in the [001] direction, replacing 1/4 of the Al2 atom. Chen et al. [37] pointed out that the vacancy in the [001] direction is an important way for Zn atoms to stay and diffuse.

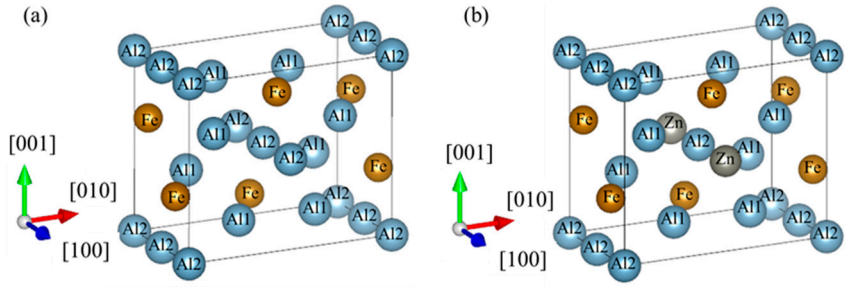


Figure 15. Calculation model of (**a**) Fe_2Al_5 and (**b**) $Fe_2Al_5Zn_x$.

As shown in Table 8, the lattice constant and formation enthalpy of Fe_2Al_5 and $Fe_2Al_5Zn_x$ after structural optimization are calculated ΔH_f. The enthalpy of the formation of both crystals is negative, indicating that the two crystal structures are thermodynamically stable. The calculated enthalpy of the formation of Fe_2Al_5 is about -16.99 kJ $\times$ mol^{-1}, which is close to that calculated by the EAM method. $Fe_2Al_5Zn_x$ shows a lower enthalpy of formation, mainly because Zn has a higher formation energy than Al. The lattice constant of $Fe_2Al_5Zn_x$ is close to that of Fe_2Al_5, but the lattice constant α increases slightly. This may be caused by the introduction of Zn atoms which destroyed the original crystal structure symmetry.

Table 8. Calculated lattice constant and formation enthalpy of Fe_2Al_5 and $Fe_2Al_5Zn_x$.

Phase	Method	a (Å)	b (Å)	c (Å)	Angle	ΔH_f (kJ $\times$ mol^{-1})
Fe_2Al_5	This work	7.476	6.214	4.741	$\alpha = \beta = \gamma = 90°$	−16.99
	EAM	7.622	6.323	4.178		−14.09 [17]
$Fe_2Al_5Zn_x$	This work	7.477	6.236	4.700	$\alpha = 90.125°$ $\beta = \gamma = 90°$	−17.62

3.4.2. Elastic Properties

The anisotropic elastic properties of Fe_2Al_5 and $Fe_2Al_5Zn_x$ are calculated. Table 9 shows the elastic constants of Fe_2Al_5 and $Fe_2Al_5Zn_x$. Fe_2Al_5 has 9 elastic constants be-

cause of its orthorhombic structure, and $Fe_2Al_5Zn_x$ has 13 elastic constants because of its monoclinic structure. Figure 16 shows the Young's modulus E and shear modulus G. The Young's modulus has a maximum value in the ⟨100⟩ crystallographic family, the shear modulus has an extreme value in the [100] and [001] crystallographic family, and a maximum value in the ⟨111⟩ crystallographic family, which is consistent with the symmetry of the orthorhombic system. The shear modulus of Fe_2Al_5 and $Fe_2Al_5Zn_x$ are basically the same, but the Young's modulus is different in the direction of [010] and [001]. After Zn is added, the Young's modulus in the direction of [010] and [001] decreases.

Table 9. Elastic constants of Fe_2Al_5 and $Fe_2Al_5Zn_x$.

Fe_2Al_5	C_{11}	C_{12}	C_{13}	C_{22}	C_{23}	C_{33}	C_{44}	C_{55}	C_{66}
	240.91	66.08	53.07	283.08	63.37	272.50	70.26	52.30	86.33
$Fe_2Al_5Zn_x$	C_{11}	C_{12}	C_{13}	C_{22}	C_{23}	C_{33}	C_{44}	C_{55}	C_{66}
	233.56	64.31	55.16	277.00	66.83	265.66	75.92	54.22	86.07
	C_{15}	C_{25}	C_{35}	C_{46}					
	4.15	−1.03	2.07	1.38					

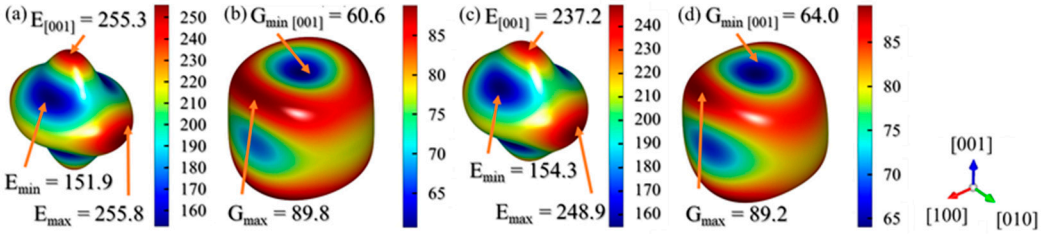


Figure 16. Calculated anisotropic elastic moduli of Fe_2Al_5 and $Fe_2Al_5Zn_x$: (**a**) Young's modulus and (**b**) shear modulus of Fe_2Al_5; (**c**) Young's modulus and (**d**) shear modulus of $Fe_2Al_5Zn_x$. (Unit: GPa).

3.4.3. Differential Charge Density

After Zn is added, the Young's modulus of the η phase decreases in the b and c directions, which can be explained by the charge distribution. Figure 17 shows the differential charge density distribution of η-Fe_2Al_5 and η-$Fe_2Al_5Zn_x$ on (100) and $(1\bar{3}0)$ crystal planes. As described by Burkhardt et al. [26], the peak of the charge distribution appears at the Fe atom. According to Figure 17a,c, the differential charge density also shows that the charge is mainly concentrated near the Fe atom, which improves the bond strength of the Fe-Al binary IMC and makes the IMC have properties similar to ceramics. Also affected by the Al atom in the [001], the high charge density region near the Fe atom is mainly arranged along the [001], and the charge distribution is non-uniform. This difference will also cause the mechanical properties of IMC to show anisotropy. The large atomic spacing and small charge density difference in the direction of a are the reasons why the Young's modulus in the direction of a is smaller than that in the direction of [010] and [001], as shown in Figure 16 above. Comparing Figure 17a,b, the charge density of Fe atoms on the (100) crystal plane decreases after the presence of Zn atoms in the channel along the [001] direction, indicating that Zn atoms also have strong binding ability on electrons. Similar phenomena can also be found on the $(1\bar{3}0)$ crystal plane by comparing Figure 17c,d.

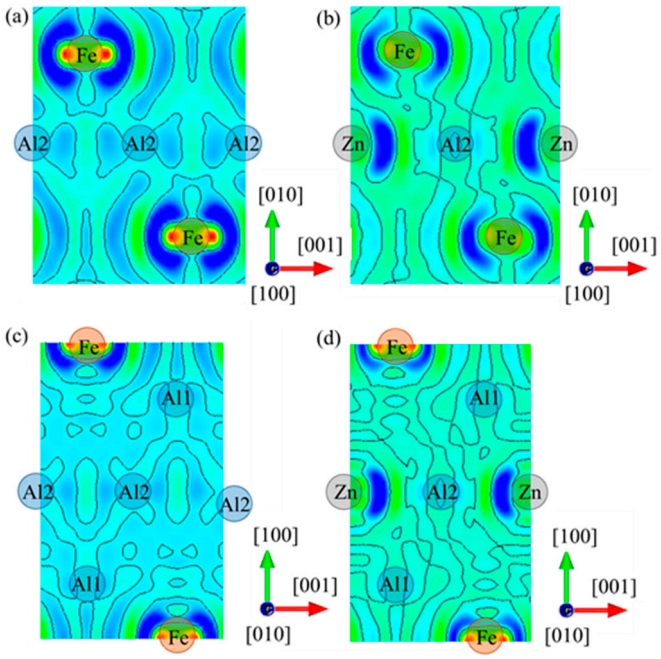


Figure 17. Differential charge density on crystal planes, (**a**) (100) plane of Fe_2Al_5, (**b**) (100) plane of $Fe_2Al_5Zn_x$, (**c**) $(1\bar{3}0)$ plane of Fe_2Al_5 and (**d**) $(1\bar{3}0)$ plane of $Fe_2Al_5Zn_x$.

4. Conclusions

In summary, this study explored the impact of the Zn content on the Al-Fe laser cladding interface. The findings indicate that adding Zn powder to the surface of the Al substrate enables the production of a continuous Fe-based cladding layer by laser cladding. However, exceeding 60 mg × cm^{-2} of applied Zn powder can limit the spread of the Fe-based cladding layer and increase the contact angle of the Fe-based cladding layer. The alloying Zn layer is useful for spreading the Fe-based cladding layer on the Al substrate.

Moreover, the results demonstrate that the Zn content at the interface is positively correlated with the amount of applied Zn powder layer. Pre-alloying increases the thickness of the η phase at the interface, with a maximum thickness of 43.6 μm. Zn is mainly enriched in the substrate, followed by the IMC layer. The Zn content is higher in the η phase compared to the θ phase in the [001] due to the vacancy of the η phase. Additionally, we found that Zn can improve the shear strength of the interface and increase the content of Zn-Al eutectic in the applied Zn layer through laser alloying, enhancing the shear strength stability. While the shear fracture is mainly a brittle fracture dominated by the η phase, there is also a localized ductile fracture between the cladding layer and the substrate. After laser alloying, the highest shear strength is obtained when the amount of applied Zn powder is 60 mg × cm^{-2}, with an average of 89.9 MPa.

Finally, based on DFT calculations, the mechanical properties of Fe_2Al_5 and $Fe_2Al_5Zn_x$ are found to be quite similar, with the Young's modulus and shear modulus in [010] and [001] being only slightly reduced. The study also found that the effect of Zn on the strength of the η phase is limited and that the introduction of Zn can improve the thickness and stability of the η phase at the Al-Fe interface. Overall, these findings provide important insights into the effect of Zn content at the Al-Fe laser cladding interface and can be useful in developing new high-performance materials for various industrial applications.

Author Contributions: Investigation and writing—original draft, K.W.; Methodology, supervision and Funding acquisition, X.Y.; Project administration, supervision and funding acquisition, C.L.; Resources and Funding acquisition, K.D. All authors have read and agreed to the published version of the manuscript.

Funding: This research was funded by National Key R&D Program of China (grant number 2018YFB2002000) and National Key R&D Program of China (grant number 2022YFB4601803).

Institutional Review Board Statement: Not applicable.

Informed Consent Statement: Not applicable.

Data Availability Statement: All data that support the findings of this study are included within the article.

Conflicts of Interest: The authors declare no conflict of interest.

References

1. Lampa, C.; Smirnov, I. High speed laser cladding of an iron based alloy developed for hard chrome replacement. *J. Laser Appl.* **2019**, *31*, 022511. [CrossRef]
2. Sadeghian, A.; Iqbal, N. A review on dissimilar laser welding of steel-copper, steel-aluminum, aluminum-copper, and steel-nickel for electric vehicle battery manufacturing. *Opt. Laser Technol.* **2021**, *146*, 107595. [CrossRef]
3. Edrisy, A.; Perry, T.; Alpas, A.T. Investigation of scuffing damage in aluminum engines with thermal spray coatings. *Wear* **2005**, *259*, 1056–1062. [CrossRef]
4. Wang, K.Y.; Xie, C.; Du, K.P.; Li, C.; Yin, X. A novel rotatable inner-surface laser cladding method. In Proceedings of the 10th International Symposium on Advanced Optical Manufacturing and Testing Technologies: Advanced and Extreme Micro-Nano Manufacturing Technologies, Chengdu, China, 13 December 2021. [CrossRef]
5. Shang, S.-L.; Sun, H.; Pan, B.; Wang, Y.; Krajewski, A.M.; Banu, M.; Li, J.; Liu, Z.-K. Forming mechanism of equilibrium and non-equilibrium metallurgical phases in dissimilar aluminum/steel (Al–Fe) joints. *Sci. Rep.* **2021**, *11*, 24251. [CrossRef] [PubMed]
6. Šlapáková, M.; Křivská, B.; Fekete, K.; Králík, R.; Grydin, O.; Stolbchenko, M.; Schaper, M. The influence of surface on direction of diffusion in Al-Fe clad material. *Mater. Charact.* **2022**, *190*, 112005. [CrossRef]
7. Zhou, D.W.; Liu, J.S.; Lu, Y.Z.; Xu, S. Effect of adding powder on joint properties of laser penetration welding for dual phase steel and aluminum alloy. *Opt. Laser Technol.* **2017**, *94*, 171–179. [CrossRef]
8. Yan, F.; Zhang, K.; Yang, B.; Chen, Z.; Zhu, Z.; Wang, C. Interface characteristics and reaction mechanism of steel/Al welds produced by magnetic field assisted laser welding-brazing. *Opt. Laser Technol.* **2021**, *138*, 106843. [CrossRef]
9. Cao, R.; Chang, J.H.; Huang, Q.; Zhang, X.; Yan, Y.; Chen, J. Behaviors and effects of Zn coating on welding-brazing process of Al-Steel and Mg-steel dissimilar metals. *J. Manuf. Process.* **2018**, *31*, 674–688. [CrossRef]
10. Peyre, P.; Sierra, G.; Deschaux-Beaume, F.; Stuart, D.; Fras, G. Generation of aluminium–steel joints with laser-induced reactive wetting. *Mater. Sci. Eng. A* **2007**, *444*, 327–338. [CrossRef]
11. Springer, H.; Szczepaniak, A.; Raabe, D. On the role of zinc on the formation and growth of intermetallic phases during interdiffusion between steel and aluminium alloys. *Acta Mater.* **2015**, *96*, 203–211. [CrossRef]
12. Nguyen, D.-S.; Park, H.-S.; Lee, C.-M. Applying Selective Laser Melting to Join Al and Fe: An Investigation of Dissimilar Materials. *Appl. Sci.* **2019**, *9*, 3031. [CrossRef]
13. Zhang, J.L.; Liu, Y.C.; Hu, C.H.; Jiang, Y.; Addad, A.; Ji, G.; Song, C.; Zhai, Q. The effect of Cr content on intragranular κ-carbide precipitation in Fe-Mn-Al-(Cr)-C low-density steels: A multiscale investigation. *Mater. Charact.* **2022**, *186*, 111801. [CrossRef]
14. Desai, P.D. Thermodynamic Properties of Selected Binary Aluminum Alloy Systems. *J. Phys. Chem. Ref. Data* **1987**, *16*, 109–124. [CrossRef]
15. Baker, H. *ASM Handbook, Volume 3: Alloy Phase Diagrams*, 10th ed.; ASM International: Phoenix, AZ, USA, 1993; pp. 293–294.
16. Liu, Y.; Chong, X.; Jiang, Y.; Zhou, R.; Feng, J. Mechanical properties and electronic structures of Fe-Al intermetallic. *Phys. B* **2017**, *506*, 1–11. [CrossRef]
17. Zhang, C.; Huang, S.; Shen, J.; Chen, N.-X. Structural and mechanical properties of Fe–Al compounds: An atomistic study by EAM simulation. *Intermetallics* **2014**, *52*, 86–91. [CrossRef]
18. Li, Y.; Liu, Y.; Yang, J. First principle calculations and mechanical properties of the intermetallic compounds in a laser welded steel/aluminum joint. *Opt. Laser Technol.* **2020**, *122*, 105875. [CrossRef]
19. Kresse, G.; Furthmüller, J. Efficient iterative schemes for *ab initio* total-energy calculations using a plane-wave basis set. *Phys. Rev. B* **1996**, *54*, 11169–11186. [CrossRef]
20. Kresse, G.; Furthmüller, J. Efficiency of ab-initio total energy calculations for metals and semiconductors using a plane-wave basis set. *Comput. Mater. Sci.* **1996**, *6*, 15–50. [CrossRef]
21. Perdew, J.P. Erratum: Density-functional approximation for the correlation energy of the inhomogeneous electron gas. *Phys. Rev. B* **1986**, *34*, 7406. [CrossRef]
22. Perdew, J.P.; Burke, K.; Ernzerhof, M. Generalized gradient approximation made simple. *Phys. Rev. Lett.* **1996**, *77*, 3865–3868. [CrossRef]
23. Chadi, D.J. Special points for Brillouin-zone integrations. *Phys. Rev. B* **1977**, *16*, 1746–1747. [CrossRef]
24. Marmier, A.; Lethbridge, Z.A.; Walton, R.I.; Smith, C.W.; Parker, S.C.; Evans, K.E. ElAM: A computer program for the analysis and representation of anisotropic elastic properties. *Comput. Phys. Commun.* **2010**, *181*, 2102–2115. [CrossRef]

25. Li, X.; Scherf, A.; Heilmaier, M.; Stein, F. The Al-Rich part of the Fe-Al phase diagram. *J. Phase Equilib. Diff.* **2016**, *37*, 162–173. [CrossRef]
26. Burkhardt, U.; Grin, Y.; Ellner, M.; Peters, K. Structure refinement of the iron–aluminium phase with the approximate composition Fe_2Al_5. *Acta Crystallogr. Sect. B* **1994**, *50*, 313–316. [CrossRef]
27. Szczepaniak, A.; Fan, J.; Kostka, A.; Raabe, D. On the Correlation Between Thermal Cycle and Formation of Intermetallic Phases at the Interface of Laser-Welded Aluminum-Steel Overlap Joints. *Adv. Eng. Mater.* **2012**, *14*, 464–472. [CrossRef]
28. Rathod, M.; Kutsuna, M. Joining of aluminum Alloy 5052 and low-carbon steel by laser roll welding. *Weld. J.* **2004**, *83*, 16S–26S.
29. Wallerstein, D.; Lusquiños, F.; Comesaña, R.; del Val, J.; Riveiro, A.; Badaoui, A.; Pou, J. Dissimilar unbeveled butt joints of AA6061 to S235 structural steel by means of standard single beam fiber laser welding-brazing. *J. Mater. Process. Technol.* **2020**, *291*, 116994. [CrossRef]
30. Ogura, T.; Wakazono, R.; Yamashita, S.; Saida, K. Dissimilar laser brazing of aluminum alloy and galvannealed steel and defect control using interlayer. *Weld. World* **2020**, *64*, 697–706. [CrossRef]
31. Sierra, G.; Peyre, P.; Beaume, F.D.; Stuart, D.; Fras, G. Galvanised steel to aluminium joining by laser and GTAW processes. *Mater. Charact.* **2008**, *59*, 1705–1715. [CrossRef]
32. Yuan, R.; Deng, S.; Cui, H.; Chen, Y.; Lu, F. Interface characterization and mechanical properties of dual beam laser welding-brazing Al/steel dissimilar metals. *J. Manuf. Process.* **2019**, *40*, 37–45. [CrossRef]
33. Ozaki, H.; Kutsuna, M.; Nakagawa, S.; Miyamoto, K. Laser roll welding of dissimilar metal joint of zinc coated steel to aluminum alloy. *J. Laser Appl.* **2010**, *22*, 1–6. [CrossRef]
34. Suder, W.J.; Williams, S.W. Investigation of the effects of basic laser material interaction parameters in laser welding. *J. Laser Appl.* **2012**, *24*, 032009. [CrossRef]
35. Xia, H.; Tao, W.; Li, L.; Tan, C.; Zhang, K.; Ma, N. Effect of laser beam models on laser welding–brazing Al to steel. *Opt. Laser Technol.* **2020**, *122*, 105845. [CrossRef]
36. Vinokur, A.I.; Hilleke, K.P.; Fredrickson, D.C. Principles of weakly ordered domains in intermetallics: The cooperative effects of atomic packing and electronics in Fe_2Al_5. *Acta Crystallogr. A* **2019**, *75*, 297–306. [CrossRef]
37. Chen, M.J.; Huang, J.K.; He, C.C.; Shi, Y.; Fan, D. Thermodynamic analysis of the formation of Fe-Al-Zn intermetallic compounds in Al/galvanized steel interface. *Acta Metall. Sinica* **2016**, *52*, 113–119. [CrossRef]

Disclaimer/Publisher's Note: The statements, opinions and data contained in all publications are solely those of the individual author(s) and contributor(s) and not of MDPI and/or the editor(s). MDPI and/or the editor(s) disclaim responsibility for any injury to people or property resulting from any ideas, methods, instructions or products referred to in the content.